

Optical spectroscopic characterizations of laser irradiated olivine grains

Yazhou Yang (杨亚洲)¹, Hao Zhang (张昊)^{1,2}, Ziwei Wang (王紫薇)¹, Ye Yuan (袁野)¹, Shaolin Li (李少林)³, Weibiao Hsu (徐伟彪)³, and Chujian Liu (刘初见)⁴

¹ Planetary Science Institute, School of Earth Sciences, China University of Geosciences, Wuhan 430074, PR China
e-mail: um_zhanghao@yahoo.com; yangyazhou1@gmail.com

² Key Laboratory of Spectral Imaging Technology, Xi'an Institute of Optics and Precision Mechanics, Chinese Academy of Sciences, Xi'an 710119, PR China

³ Purple Mountain Observatory, Chinese Academy of Sciences, Nanjing, PR China

⁴ State Key Laboratory of Geological Process and Mineral Resources, China University of Geosciences, Wuhan, PR China

Received 16 July 2016 / Accepted 11 October 2016

ABSTRACT

Context. Visible and near-infrared spectra of asteroids are known to be susceptible to nanophase irons produced by space weathering processes, thus making mineral identifications difficult. Mid-infrared spectroscopy may retain more mineral features owing to its lattice vibrational nature.

Aims. We investigate the structure and reflectance spectral feature changes of olivine grains before and after simulated space weathering.

Methods. We irradiate olivine grains by using pulsed laser to simulate varying degrees of micrometeorite bombardments. Reflectance measurements from 0.5 to 25 μm and radiative transfer calculations were carried out in order to compare them with each other.

Results. Both the experimental simulations and modeling results indicate that the mid-infrared spectral features of olivine grains can survive the intense irradiations. Although the Christiansen Feature is slightly shifted to longer wavelength, major vibrational bands remain essentially unchanged, because the lattice structure is quite immune to even the strongest irradiations, as revealed by both the X-ray diffraction and Raman scattering measurements.

Conclusions. Mid-infrared spectroscopy is much more immune to productions of nanophase irons and amorphous materials and thus may be used more reliably in remote detections of minerals on asteroid surfaces.

Key words. methods: laboratory: solid state – techniques: spectroscopic – radiative transfer – planets and satellites: surfaces – infrared: general – planets and satellites: composition

1. Introduction

Visible and near-infrared (VNIR) reflectance spectroscopy has been widely used in characterizing the surface mineralogical compositions of airless bodies as most silicate minerals have diagnostic absorption features in the VNIR region (e.g., Chapman 1996, 2004; Gaffey 2010). However, space weathering processes including micrometeorite impacts and ion implantations may darken and redden the VNIR spectra, reduce the spectral contrast, and thus make the spectral interpretations difficult (e.g., Hapke 2001; Chapman 2004; Nesvorný et al. 2005). Both laboratory simulations and returned-sample analysis have demonstrated that nanophase iron particles (npFe⁰), produced by the redeposition of vapor generated by the sputtering of solar wind particles and micrometeorite impacts (e.g., Hapke et al. 1975; Keller & McKay 1993; Hapke 2001), are mainly responsible for the optical effects of space weathering (e.g., Keller & McKay 1993; Pieters et al. 2000; Taylor et al. 2001; Sasaki et al. 2001, 2002, 2003; Brunetto et al. 2006; Loeffler et al. 2008; Britt et al. 2014).

Currently, laboratory simulations of space weathering can be categorized into three main types: pulsed laser is used to irradiate analog materials to simulate effects of micrometeorite impacts

(e.g., Yamada et al. 1999; Sasaki et al. 2001; Brunetto et al. 2006); proton and ion implantations are used to simulate solar-wind irradiations (e.g., Hapke 1973; Yamada et al. 1999; Brucato et al. 2004; Marchi et al. 2005; Fulvio et al. 2012; Miller et al. 2014; Kuhlman et al. 2015); and thermal treatment is also used to simulate the production of npFe⁰ (e.g., Tang et al. 2012). Recently, Kohout et al. (2014) developed a double heating method to produce npFe⁰ in a controlled way. Among these methods, pulsed laser irradiation is very effective in producing the spectral effects of space weathering as the short pulse can deliver energy in a very short timescale which is believed to be comparable to the impact duration of micrometeorites (e.g., Yamada et al. 1999).

The effects of npFe⁰ on VNIR spectra have been thoroughly studied since the confirmation of its existence on returned lunar regolith particles. Because the VNIR features below 2.5 μm in olivine and pyroxene spectra are mainly caused by electronic transitions of ferrous ions in crystal field (Burns 1993), the VNIR spectra may be greatly affected by the production of npFe⁰. The VNIR spectral effects of the npFe⁰ with varying contents, distributions, and particle sizes have been studied by using the Hapke radiative transfer model with some success (e.g., Hapke 2001; Lawrence & Lucey 2007; Denevi et al. 2008). In

contrast, space weathering effects on reflectance bands at longer wavelengths caused by thermal lattice vibrations are less well studied, but may contain rich information on space weathered minerals (Lucey et al. 2016). Early studies before modern space weathering simulations were carried out show that space weathering causes little mid-infrared (MIR) spectral changes (Salisbury et al. 1997), though this view was challenged recently (Lucey et al. 2016).

In the far-infrared region where the radiation wavelength is longer than $25 \mu\text{m}$ (wavenumber below 400 cm^{-1}), the reflectance peaks are caused by external lattice modes such as the relative motions between the ferrous ions and the SiO_4 group. Reflectance bands in the MIR from $10 \mu\text{m}$ to $25 \mu\text{m}$ (1000 to 400 cm^{-1}) are the so-called fundamental vibrational modes (Poulet & Mathieu 1976) that can be divided into internal stretching, bending and librating of the SiO_4 group. In the short wavelength infrared (SWIR) region roughly between $2.5 \mu\text{m}$ and $10 \mu\text{m}$, reflectance peaks are mainly overtones and combination bands of the fundamental lattice modes. As a result, spectral features within these regions could be less susceptible to the production of npFe^0 and hence could be potentially useful in identifying the mineralogical compositions of the surfaces of airless bodies.

In the MIR region, some prominent spectral features such as the Christiansen feature (CF), the Reststrahlen bands and the transparency feature (TF) may be used as diagnostic features of mineral compositions (e.g., Mustard & Hays 1997; Pieters 1998). The CF of silicates, manifesting itself as the reflectance minimum between 7.5 and $9 \mu\text{m}$, occurs near the Christiansen wavelength where the real part of refractive index approaches unity (e.g., Mustard & Hays 1997; Hapke 2012). The reststrahlen bands in silicates include one stronger band between 8.5 and $12 \mu\text{m}$ and one less strong band between 16.5 and $25 \mu\text{m}$, caused by Si-O stretching and Si-O-Si bending vibrations, respectively (e.g., Noel et al. 2006). The TF is a reflectance maximum located in a volume-scattering region between the two reststrahlen bands described above. The CF and TF are correlated with each other and are both dependent on compositions (e.g., Hapke 2012).

Although observational data above $2 \mu\text{m}$ are mostly thermal emission spectra, reflectance spectroscopy is a powerful and convenient tool in the laboratory to study mineral optical properties. Furthermore, the emission and reflectance spectra contain the same spectral features and are complementary through the Kirchhoff's law (Hapke 2012), and thus MIR reflectance spectroscopy is widely used to understand minerals' micro-structures (e.g., Pieters 1998, 2002). Another benefit of using the MIR spectroscopy is that it may potentially provide complementary information to the VNIR spectra. For example, Beichman et al. (2005) identified crystalline olivine based on the diagnostic features between 8 and $35 \mu\text{m}$. In addition, it has been found that some VNIR spectroscopically similar asteroids display distinctive spectral features in the MIR (Vernazza et al. 2010).

To understand the MIR characteristics of planetary analog materials before and after space weathering, we carried out pulsed laser irradiation simulations and reflectance measurements of olivine grains. In order to understand the simulation results semi-quantitatively, we also performed reflectance model predictions by using both a semi-empirical reflectance model (Hapke 2012) and a strict numerical radiative transfer model (Stamnes et al. 2000). We first present the simulation experimental procedures and the modeling methods, followed by results and discussion sections.

Table 1. Chemical composition of the original and the VDM processed olivine samples.

Major elements	Original olivine (wt. %)	Olivine processed with VDM (wt. %)
SiO_2	40.660	40.980
Al_2O_3	0.340	0.230
* TFe_2O_3	9.760	9.780
MgO	48.000	48.590
CaO	0.056	0.042
Na_2O	0.008	0.010
K_2O	0.004	0.003
TiO_2	0.011	0.005
P_2O_3	0.005	0.012
MnO	0.110	0.110
H_2O	0.040	0.040
Total	98.994	99.802
** Fo#	95	95

Notes. (*) Total iron; (**) Mg-number.

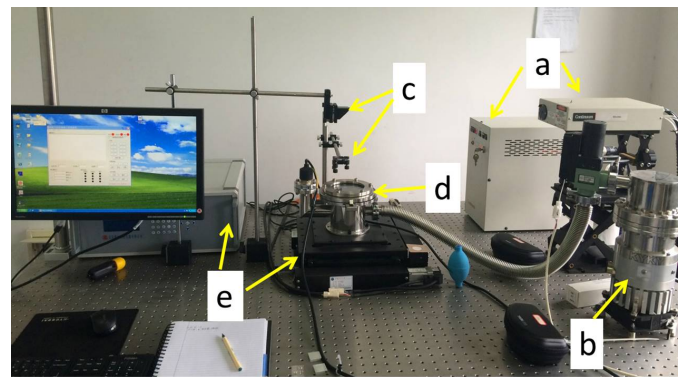


Fig. 1. Experimental setup of pulsed laser irradiations. a) Nd:YAG pulsed laser; b) molecular pump; c) reflector and optical lens; d) vacuum chamber; e) motorized X-Y translation stage and the controller.

2. Materials and methods

2.1. Experimental procedure

Samples. Olivine, a common mineral found in many meteorites and S-type asteroids (e.g., Chapman 1996, 2004), was used as the analog material in this work. Natural pure olivine granules collected from Hebei Province, China, were first grinded into a size distribution of $0 \sim 75 \mu\text{m}$ with a Vibratory Disc Mill (VDM). The olivine powders were then sieved and those smaller than $45 \mu\text{m}$ were separated as the target sample. The chemical compositions of these olivine powders were analyzed with wet chemistry method. To ensure that no contaminations were introduced during the grinding process, compositional measurements were made on both the original samples and the powders processed with the VDM. The contents of major elements of these two samples, as summarized in Table 1, indicate that the grinding process did not introduce any contaminations of iron, and the Mg number of the olivine sample is 95 (Fo_{95}).

Pulsed laser irradiations. Figure 1 shows the irradiation system used in our simulation experiments (Yamada et al. 1999; Sasaki et al. 2001). A 1064 nm Continuum Minilite II nanosecond pulsed laser with incident energy per pulse from 1 to 50 mJ

was used to simulate the micrometeorite bombardment process. After being focused by a thin lens, the laser beam diameter is reduced from 3 mm to 0.5 mm to increase the energy density. The pulse duration is 6 ~ 7 nanoseconds which is believed to be comparable with the timescale of real micrometeorite impacts (Yamada et al. 1999). Samples were placed in aluminum holders in the vacuum chamber under a pressure of 10^{-3} Pa. To remove moisture in the samples as much as possible, the powdery sample was baked for more than 5 h under 120 °C in a vacuum oven before each irradiation was carried out. Each time 0.2 g of olivine powders were uniformly placed on a 25 mm × 25 mm square area. A thin glass slide was used to cover the holder to prevent the sputtering of the powders. The chamber was installed on a motorized X–Y translation stage which is controlled by a computer. By programming the stage movement the powdery samples can be uniformly irradiated. In this work, samples were irradiated with a frequency of 15 Hz and a scanning velocity of 1 mm per second. By changing the pulse energy and number of irradiations, products with different weathering degrees can be obtained. Two pulse energy levels, 25 and 50 mJ/pulse, were used, yielding a total energy density of 750 and 1500 mJ/mm² for one irradiation experiment, respectively. We chose these two energy levels for the following reason. For an airless body located at 1 AU, the impact energy imparted by a 1 μm dust particle with mass of 10^{-12} g moving at 20 km s⁻¹ towards its surface is about 2×10^{-4} mJ (Yamada et al. 1999), giving an energy density of ~250 mJ/mm² which is equivalent to that of one single 50 mJ pulse in our experiments. Therefore, with a frequency of 15 Hz, even the 25 mJ level should be strong enough to simulate both lunar and asteroidal space weathering styles caused by micrometeorite bombardment (e.g., Yamada et al. 1999; Sasaki et al. 2001).

Reflectance measurements. After laser irradiations, the powdery sample was removed from the vacuum chamber immediately to have its VNIR and MIR reflectance spectra measured by a Bruker Vertex 70 Fourier transform infrared spectrometer equipped with Easy Diffuse accessories from Pike Technologies. The VNIR spectra were calibrated with a Labsphere Spectralon plaque with a 99% nominal reflectance in the visible. For MIR measurements, a gold mirror was used as the reference as the Spectralon has numerous absorption peaks in this spectral region. Both the VNIR and MIR spectra were measured under a biconical configuration with both the incident and viewing zenith angles spanning within the range between 40° to 65°. To reduce any possible spectral variations caused by surface inhomogeneities and packing structures, the sample holder was rotated 90 degrees after each measurement and altogether four measurements were made. When the maximum difference among the four measurements was within 5%, the measurements were deemed as reliable and the average of the four was used as the final result; otherwise a new surface was made to be measured.

Structural and compositional analysis. To verify the microscopic changes of the olivine particles, we performed structural analysis on some irradiated samples by using a Titan G2 60–300 Transmission Electron Microscope (TEM) equipped with an Energy Dispersive Spectrometer (EDS). We adopted the ultrasonic dispersion method by adding the powdery sample into anhydrous ethanol to prepare samples for TEM analysis.

In addition to the TEM observations, we also performed powder X-ray Diffraction (XRD) and Raman spectroscopic measurements for all the olivine samples to check any possible

crystal structural changes. The XRD measurements were done on a Bruker AXS D8-Focus X-ray Diffractometer. Raman scattering was carried out by using a Thermo Scientific DXR micro-Raman system with a spectral resolution of 1.5–2 cm⁻¹. The excitation laser wavelength was 532 nm and the incident power was varied from 1 to 9 mW to exclude any possible laser power dependent spectral changes.

2.2. Reflectance spectra modeling

Based on the results of our simulation experiments and previous studies, we performed reflectance model predictions to understand the spectral feature changes. npFe⁰ bearing rims on returned lunar (Keller & McKay 1997) and asteroid Itokawa (Noguchi et al. 2011) regolith particles are now known to be responsible for the spectral changes of darkening and reddening. Laboratory simulations with analog materials have successfully reproduced npFe⁰ production and the incurred reddening and darkening effects on VNIR spectra (e.g., Yamada et al. 1999; Sasaki et al. 2001; Brunetto et al. 2006). In addition to npFe⁰, a glassy coating or amorphous layer is also produced during space weathering processes (Keller & McKay 1997; Noguchi et al. 2011; Berger & Keller 2015). To understand the spectral effects of these two factors, we have performed reflectance model predictions using the Hapke photometric model (Hapke 2012) and a strict numerical algorithm, the discrete ordinate radiative transfer (DISORT) model (Stamnes et al. 2000).

The Hapke model used here (Hapke 1981) is a simplified version without the opposition effect as the current spectroscopic measurements were made at large phase angles. In this work, the bidirectional reflectance r is expressed as

$$r(i, e, g) = \frac{\omega}{4\pi} \frac{\mu_0}{\mu_0 + \mu} [p(g) + H(\gamma, \mu_0)H(\gamma, \mu) - 1], \quad (1)$$

where i , e , and g are the incidence, emission, and phase angles, respectively. $\mu_0 = \cos(i)$, $\mu = \cos(e)$, ω is the single scattering albedo, $p(g)$ is the particle phase function, and $H(\gamma, \mu)$ is the Ambartsumian–Chandrasekha H function. An analytic approximation of $H(\gamma, x)$ is given by

$$H(\gamma, x) \approx \frac{1 + 2x}{1 + 2\gamma x}, \quad (2)$$

where γ is the albedo factor defined as

$$\gamma = \sqrt{1 - \omega}. \quad (3)$$

If the single scattering quantities ω and $p(g)$ are known, other terms related to ω can be calculated and then we can obtain the reflectance quantities. In this work, we present both the model data and measurements in terms of reflectance defined as the ratio of the sample's bidirectional reflectance to that of a perfect Lambertian surface,

$$\text{Reflectance} = \frac{r(i, e, g)\pi}{\mu_0}. \quad (4)$$

Since the performance of the Hapke model has been in constant debate (e.g., Zhang & Voss 2011; Shkuratov et al. 2012; Hapke 2013), we also employed the DISORT program which numerically solves the radiative transfer equation and can achieve very high numerical precisions with enough “streams” (Stamnes et al. 2000). Although it was mainly intended for scattering media with negligible close packing effects such as atmospheric

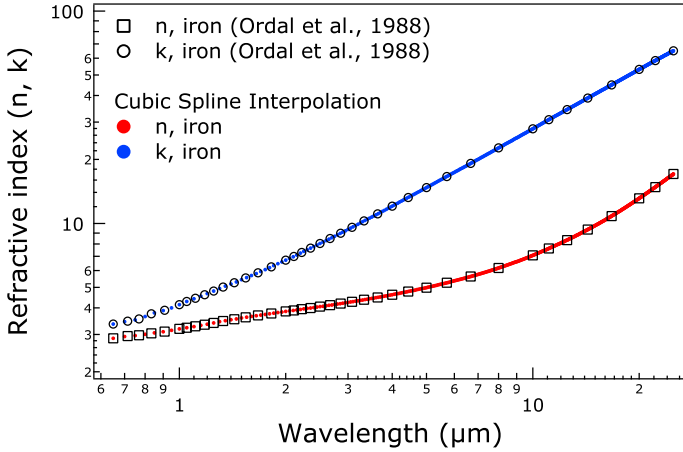


Fig. 2. Original and interpolated refractive indices n (real part) and k (imaginary part) of iron (Ordal et al. 1988).

aerosols, it was found to be able to predict reflectance measurements on closely packed transparent spherical particles very well except in the backscattering direction (Zhang & Voss 2011). We incorporate both the semi-empirical model and the strict numerical model to better understand reflectance predictions on laser irradiated grains.

The single scattering quantities ω and $p(g)$ needed by both models were computed by Mie algorithm (Mishchenko et al. 1999) for uniform particles, and the BART code (Quirantes & Bernard 2004) for grains coated with amorphous layers or npFe^0 rim, respectively. The input parameters of both codes include complex refractive indices and particle size distribution parameters. The representative particle size used in this study was assumed to be $30 \mu\text{m}$ in diameter. The refractive index data of olivine, amorphous materials (silicate glass) and metal iron needed in the calculations are from Fabian et al. (2001), Dorschner et al. (1995), Jäger et al. (1994), and Ordal et al. (1988), respectively. To achieve a higher spectral resolution, the original sparse discrete and unevenly spaced data points were interpolated to a spectral resolution of $0.05 \mu\text{m}$ between 0.65 and $25 \mu\text{m}$ using the cubic spline interpolation algorithm. Figure 2 shows the original and interpolated refractive indices of iron. Figure 3a shows the interpolated n and k data of four different silicate glasses, two pyroxene (Glass 1: $\text{Mg}_{0.95}\text{Fe}_{0.05}\text{SiO}_3$, Glass 2: $\text{Mg}_{0.4}\text{Fe}_{0.6}\text{SiO}_3$) and two olivine (Glass 3: Mg_2SiO_4 , Glass 4: $\text{Mg}_{0.8}\text{Fe}_{1.2}\text{SiO}_4$) types. We considered two pyroxene glass coating types in addition to two olivine types because during melting and evaporations the coating compositions might change. Since olivine belongs to orthorhombic symmetry, its refractive indices in the MIR vary with different orientations. Figures 3b, c show the n and k data along three crystallographic axes x , y and z of Fo_{95} olivine (Fabian et al. 2001). We made computations with these optical constants of x , y and z axes, and use their average to approximate the reflectance of randomly orientated crystals (e.g., Brucato et al. 2004).

For particles with uniformly distributed npFe^0 , we calculated the refractive index based on the Maxwell-Garnet effective medium theory (e.g., Bohren & Huffman 2008; Hapke 2001) as

$$m^2 = m_h^2 + \frac{3\Phi_{\text{Fe}}m_h^2 \left[\frac{m_{\text{Fe}}^2 - m_h^2}{m_{\text{Fe}}^2 + 2m_h^2} \right]}{1 - \Phi_{\text{Fe}} \left[\frac{m_{\text{Fe}}^2 - m_h^2}{m_{\text{Fe}}^2 + 2m_h^2} \right]}, \quad (5)$$

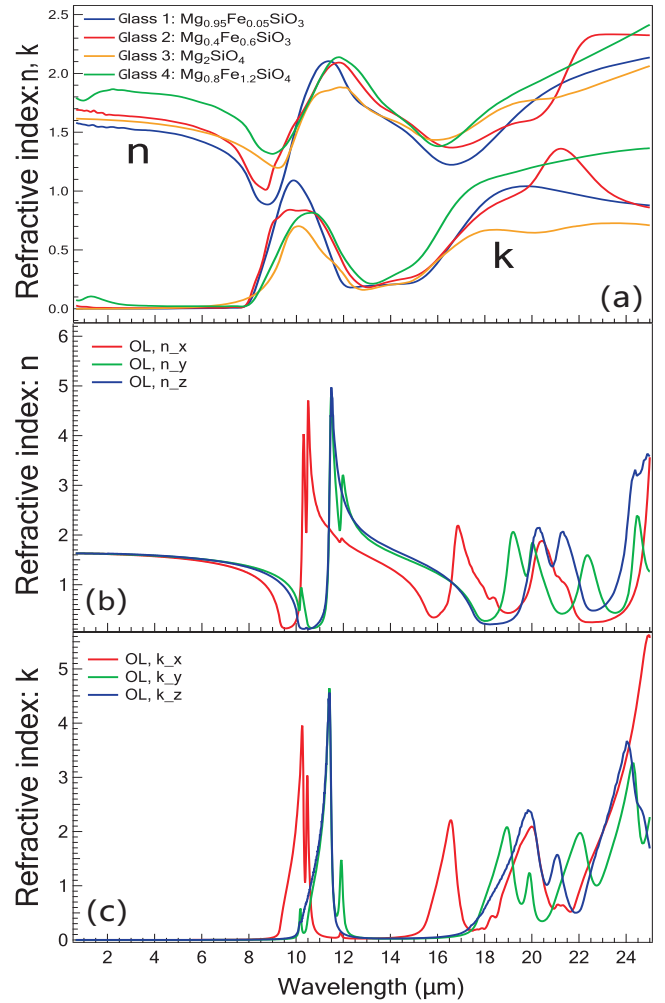


Fig. 3. Interpolated refractive indices n and k of olivine and four different silicate glasses. **a)** n , k data of Glass 1 and Glass 2 from Jäger et al. (1994); Glass 3 from Fabian et al. (2000); and Glass 4 from Dorschner et al. (1995); **b)** n data of olivine from Fabian et al. (2001); **c)** k data of olivine from Fabian et al. (2001). x , y and z indicate three different crystallographic axes.

where m is the effective complex refractive index, $m_h = n_h + ik_h$ and $m_{\text{Fe}} = n_{\text{Fe}} + ik_{\text{Fe}}$ are the refractive indices of host material and iron, respectively, Φ_{Fe} is the volumetric fraction of the npFe^0 .

3. Results

3.1. Experimental results

Figure 4 shows the original olivine sample and three typical samples irradiated with different pulse energy levels (25 and 50 mJ) and duration combinations (2 and 5 times). When compared to the original fresh white sample (Fig. 4a), one easily sees the albedo reduction of samples irradiated under 25 mJ/pulse for 2 times (Fig. 4b). With the increase in energy level and number of irradiations, the darkening effect becomes stronger. As an extreme, the sample irradiated with 50 mJ/pulse for 5 times becomes charcoal black (Fig. 4d).

Reflectance spectra. The VNIR reflectance spectra of seven olivine samples irradiated with varying degrees and the unirradiated one are shown in Fig. 5, while the same spectra normalized at 750 nm are shown in Fig. 6. After irradiations the

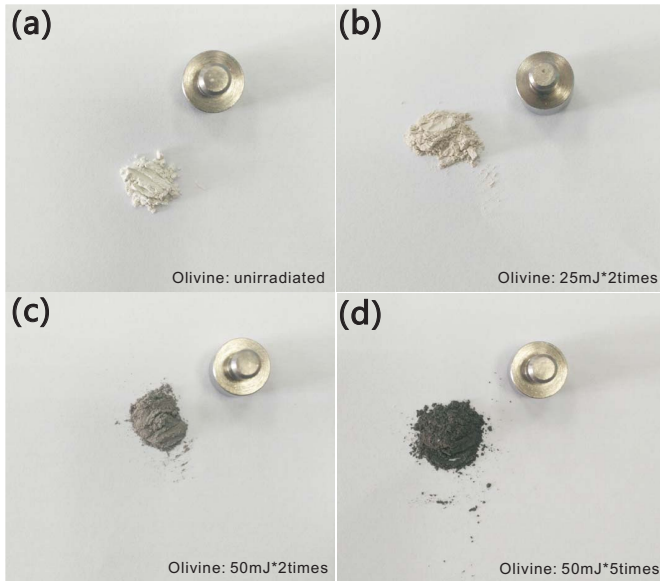


Fig. 4. Typical olivine powders before and after irradiations with different pulse energy levels and number of irradiations. **a)** Original olivine sample; **b)** after irradiation with 25 mJ/pulse for 2 times; **c)** after irradiation with 50 mJ/pulse for 2 times; **d)** after irradiation with 50 mJ/pulse for 5 times. The sample holder used in reflectance measurement is also shown as a reference.

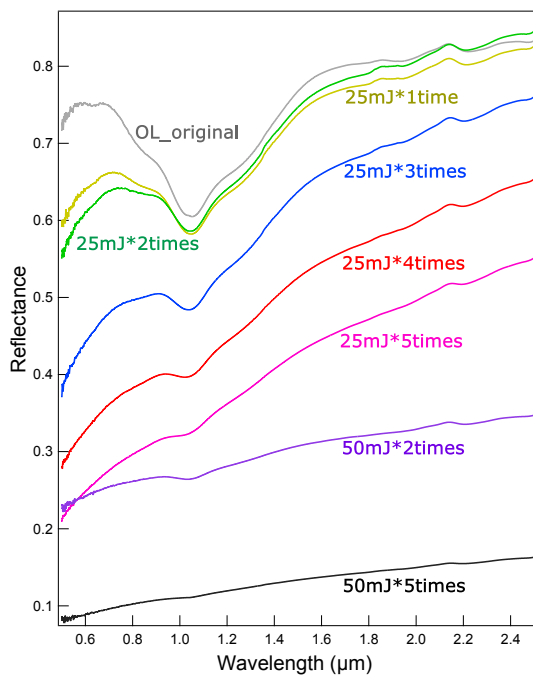


Fig. 5. VNIR reflectance spectra of olivine samples before and after irradiations. Eight spectra: non-irradiated, irradiated under 25 mJ/pulse for 1 to 5 times, irradiated under 50 mJ/pulse for 2 and 5 times. All spectra are measured relative to a Spectralon standard with 99% nominal reflectance.

VNIR spectra of olivine show the well-known darkening and reddening changes (e.g., Yamada et al. 1999; Sasaki et al. 2001). We characterize the VNIR spectral changes by using three types of parameters: the reflectance values at 600 nm and 1700 nm are used to describe the darkening effect in the visible and near-infrared (NIR) regions; the ratio of reflectance values at 1700 nm and 750 nm is used to characterize the reddening effect; the depth of the 1 μm absorption band is used to evaluate

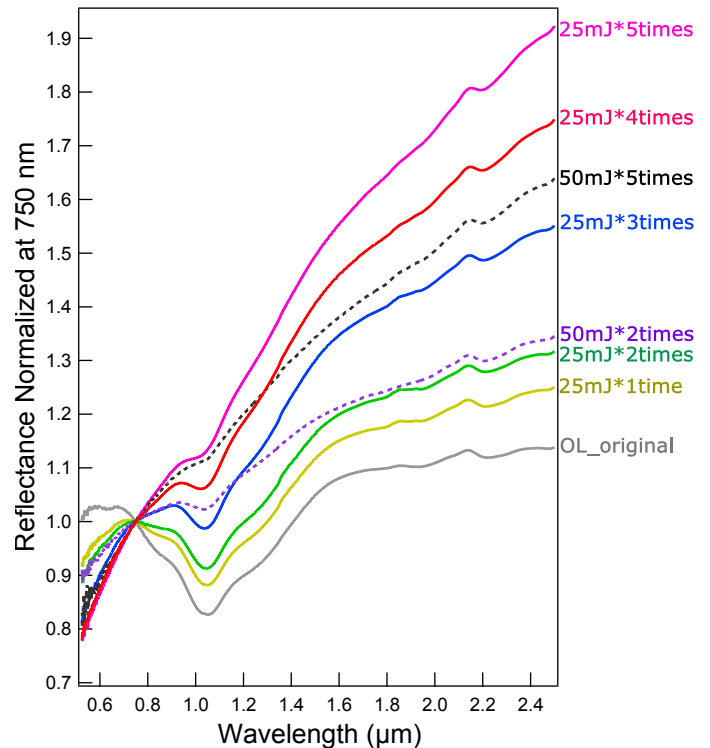


Fig. 6. VNIR reflectance spectra of olivine samples normalized at 750 nm.

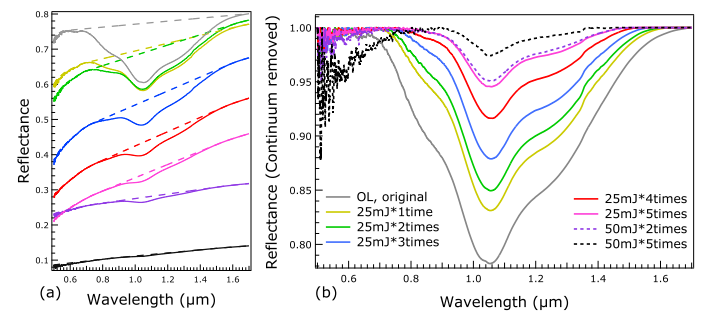


Fig. 7. Reflectance spectra before and after removing the continuum. **a)** The original spectra (solid) and the continua used as the baselines (dashed) obtained by fitting the peaks between 0.5 and 1.7 μm ; **b)** the continuum-removed spectra.

the decrease in spectral contrast. The band depth is estimated from the continuum-removed spectra (Fig. 7) by subtracting the minimum reflectance value within the absorption band from unity (Clark & Roush 1984). We limit the VNIR feature discussions in the spectral region 500 ~ 1700 nm as the spurious peak at 2.14 μm caused by Spectralon absorption (Zhang et al. 2014) would affect the shape of the baseline. All VNIR spectral changes are summarized in Table 2.

Compared with the original olivine spectrum, all irradiated sample spectra show more reductions of reflectance in the visible than in the NIR. The normalized spectra shown in Fig. 6 are redder with the increase in number of irradiations. The depth of the 1 μm absorption band of the original sample is 0.218 (Table 2) and it dropped to 0.054 and 0.049 after being irradiated under 25 mJ/pulse for 5 times and 50 mJ/pulse for 2 times, respectively. After being irradiated with 50 mJ/pulse for 5 times, the overall reflectance value decreased by more than 70%, and the 1 μm absorption feature almost disappeared completely (over irradiated). Irradiation with 50 mJ/pulse for 2 times caused more

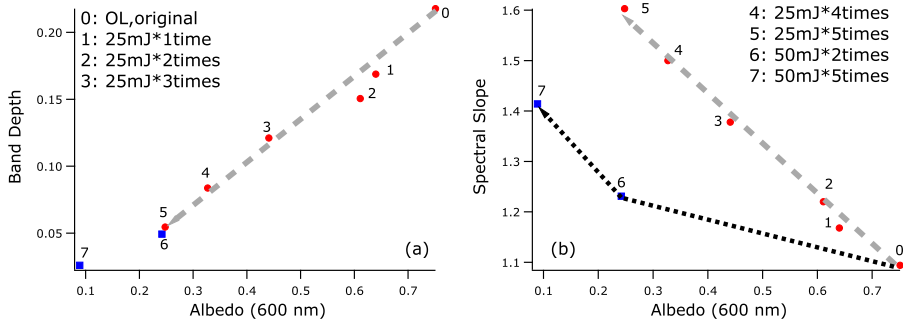


Fig. 8. Variations of the $1\ \mu\text{m}$ band depth and the VNIR spectral slope of olivines with the increased number of irradiations. **a)** The $1\ \mu\text{m}$ band depth vs. albedo at $600\ \text{nm}$; **b)** the spectral slopes vs. albedo. The arrow at the end indicates the increase in irradiation levels.

Table 2. Parameters characterizing the VNIR spectral features of olivines before and after irradiations.

Olivine samples	Albedo		Band depth	Reddening $R(1700)/R(750)$
	600 nm	1700 nm		
Original	0.751	0.801	0.218	1.094
25 mJ \times 1 time	0.640	0.771	0.169	1.168
25 mJ \times 2 times	0.611	0.783	0.150	1.220
25 mJ \times 3 times	0.441	0.675	0.121	1.378
25 mJ \times 4 times	0.327	0.561	0.084	1.500
25 mJ \times 5 times	0.248	0.460	0.054	1.603
50 mJ \times 2 times	0.242	0.318	0.049	1.231
50 mJ \times 5 times	0.089	0.141	0.026	1.414

prominent darkening than that with 25 mJ/pulse for 5 times did, especially in the NIR region.

Figure 8 shows how the band depth and spectral slope of the VNIR spectra change with the increase in number of irradiations. The spectral slope, albedo and band depth almost reduced simultaneously under irradiation with 25 mJ/pulse, corresponding to a typical lunar style weathering (Gaffey 2010). In contrast, irradiation with a higher energy level (50 mJ/pulse) caused a quicker decrease in albedo and band depth and the decreases are not proportional to the number of irradiations.

It is noted that irradiations with 25 mJ for 2 times produced little band depth changes and the NIR reflectance above $1.2\ \mu\text{m}$ even slightly increased as compared with irradiation with 25 mJ for 1 time. Repeated experimentations show that although the visible albedo at this irradiation level does decrease, the NIR albedo is very close to sample irradiated with 25 mJ for 1 time. It is likely that when the irradiation levels are low, the darkening effect in the NIR is not significant.

In contrast to the VNIR spectra, nearly all major MIR spectral features are retained as shown in Fig. 9, even after the heaviest irradiations. The sharp peak centered around $3\ \mu\text{m}$ in Fig. 9a was caused by the absorption of the reference gold mirror. The CF of the original sample around $9.0\ \mu\text{m}$ only slightly darkens without appreciable widening after irradiations with 25 mJ/pulse for 1 to 5 times, while irradiation with 50 mJ/pulse further broadens the CF peak. Even after the heaviest irradiation (50 mJ \times 5 times), the CF position of olivine only slightly shifted to longer wavelength. The central wavelength of the TF between $12\text{--}15\ \mu\text{m}$ only shifted to the shorter wavelength by $\sim 0.13\ \mu\text{m}$ ($8\ \text{cm}^{-1}$) after irradiation with 50 mJ/pulse for 5 times, whereas the change is negligible for olivines irradiated with 25 mJ/pulse for 1–5 times. The restrahlen bands of olivine are weakened by the irradiation, but all the vibrational modes are identifiable after irradiations. More discussions on MIR features are deferred to Sect. 4.

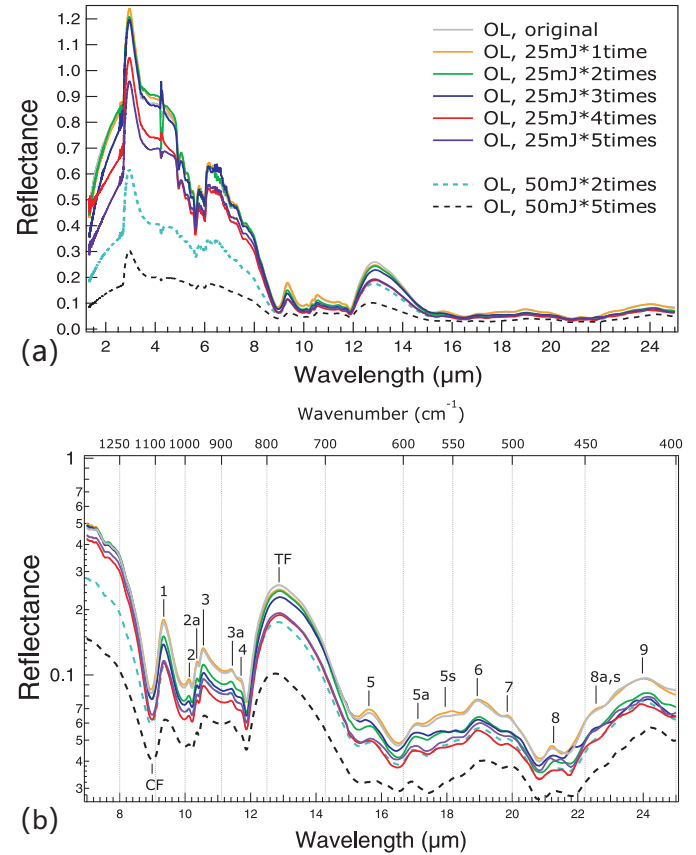


Fig. 9. MIR reflectance spectra of olivine samples before and after irradiations in decimal scale **a)** and logarithmic scale **b)**. The MIR spectra were measured relative to a gold mirror standard and then scaled to the VNIR value in the overlapping region. CF: the Christiansen Feature; TF: the Transparency Feature. The numbers indicating the vibrational modes are summarized in Table 3 in Hamilton (2010).

TEM and EDS analysis. Figure 10 shows the bright field TEM images of olivines irradiated under 50 mJ for 2 times. The presence of spherical particles with diameters less than $500\ \text{nm}$ present on the surface of the large olivine particle (Fig. 10a) indicate that melting and redeposition processes may have occurred during the irradiations. We selected two regions of interest (ROI) as indicated by the white boxes shown in Fig. 10a to study their structures and compositions. Figure 10b is the enlarged image of ROI 1 with many nanophase particles ($5\text{--}20\ \text{nm}$) uniformly distributed near the surface. On the rim of ROI 2 we can find similar dark nanophase particles (Fig. 10c) smaller than $10\ \text{nm}$. In order to check if the nanophase particles are npFe^0 or not, we performed EDS mapping of some major elements. Figure 11a is the enlarged dark field TEM image of ROI 1 with

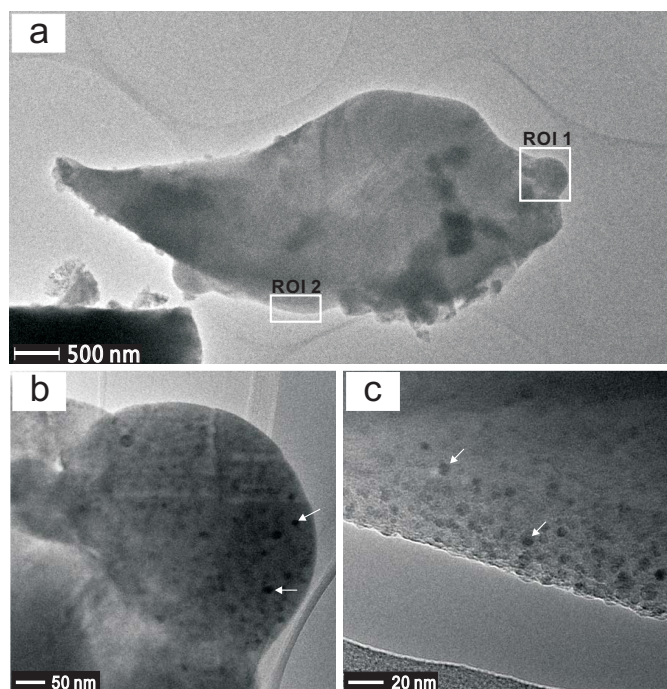


Fig. 10. Bright field TEM images of olivine samples after being irradiated under 50 mJ/pulse for 2 times. **a)** One single olivine particle with two ROIs indicated by the white boxes; **b)** and **c)** are the enlarged images of ROI 1 and ROI 2, respectively. The white arrows in **b)** and **c)** indicate the presence of nanophase particles.

the elemental mapping area indicated by the orange box. In contrast to the bright field image (Fig. 10), the nanophase particles look bright in the dark field image (Fig. 11a). As shown in Fig. 11b, elements Si, O and Mg are uniformly distributed in the mapping area, while Fe shows an abnormal distribution feature. The Fe-rich spots are consistent with those nanophase particles shown in Fig. 10b and hence the nanophase particles are identified as npFe^0 . From the TEM images of olivines irradiated with 50 mJ/pulse for 2 times, we found that some olivine particles are covered by an amorphous layer. Figure 12 shows the bright field TEM images of one typical olivine particle with a ~ 10 nm thick layer. In the high resolution TEM image (Fig. 12b), the inner part of the particle show clear lattice fringes, while the layer does not. This does not imply, however, that 10 nm is the average or maximum thickness of the produced amorphous layers in our experiments.

Figure 13 shows the TEM images and EDS mapping results of a typical olivine sample irradiated under 50 mJ/pulse for 5 times, the heaviest irradiation dose in this study. The diameters of the npFe^0 range from 5 to 30 nm, about 10 nm larger than those in the sample irradiated under 50 mJ/pulse 2 times.

For irradiations at lower energy levels (25 mJ), the npFe^0 particles produced have lower concentrations than that irradiated at 50 mJ and are more difficult to be found in TEM observations. However, the size of the iron grains produced is about the same as that produced by irradiations with 50 mJ. Figure 14 compares the TEM images of olivine grains irradiated with 25 mJ and 50 mJ for 2 times, respectively. It is seen that the npFe^0 grains have similar size distributions and are all smaller than 30 nm.

XRD analysis. Figure 15 shows the XRD results of three typical olivine samples. The positions of all main diffraction peaks

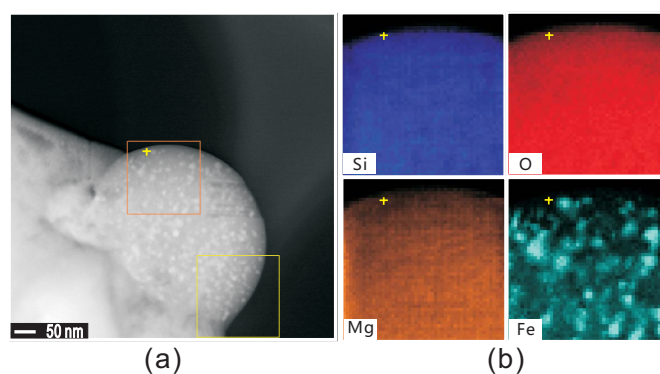


Fig. 11. EDS mapping of major elements Si, O, Mg and Fe. **a)** Dark field image of the ROI 1 in Fig. 10a with the orange box indicating the EDS mapping region. The area surrounded by the yellow box is used for drift corrections; **b)** EDS mapping results of Si, O, Mg and Fe. The brightness of the pixels is correlated with the relative abundance of the corresponding element. The brighter spots in the Fe distribution map are consistent with the white spots in the enclosed area of the orange box, showing that the nanoparticles are indeed nanophase irons.

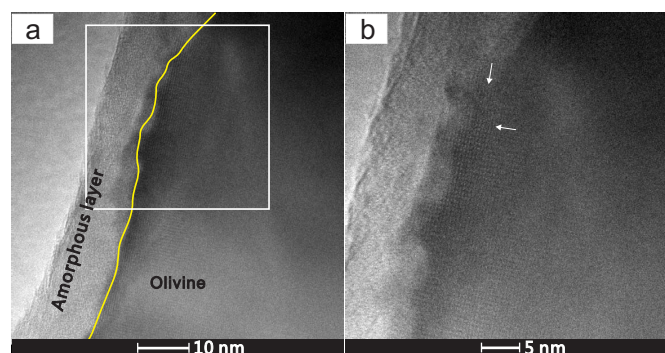


Fig. 12. Typical bright field TEM images of the olivine sample after irradiation with 50 mJ/pulse for 2 times. **a)** A yellow curve indicating the boundary between the amorphous layer and the olivine crystal; **b)** the high resolution image of the enclosed area of the white box in **a)**, showing the olivine lattice fringes indicated by the white arrows.

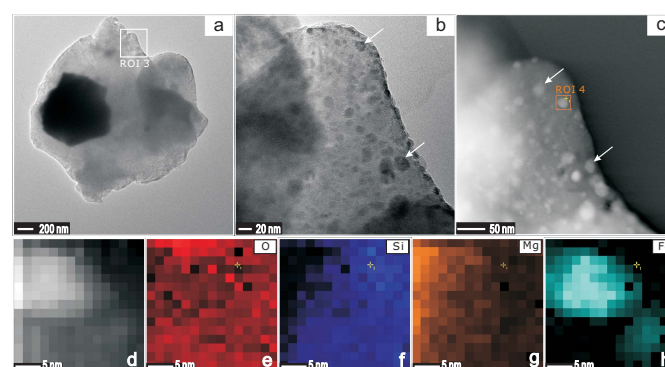


Fig. 13. TEM image and EDS mapping results of the olivine sample irradiated under 50 mJ for 5 times. **a)** Bright field image of one olivine particle; **b)** the enlarged image of ROI 3 as indicated by the white box in **a)**; **c)** the dark field image of ROI 3, and ROI 4 is the region selected for EDS mapping; **d)** the high resolution image of ROI 4; **e)–h)** EDS mapping results of four major elements: O, Si, Mg, and Fe.

determined by the atomic distance within the mineral structure remain unchanged even after the heaviest irradiation with 50 mJ/pulse for 5 times. Phase analysis demonstrates that no obvious phase changes were incurred by irradiations. Although

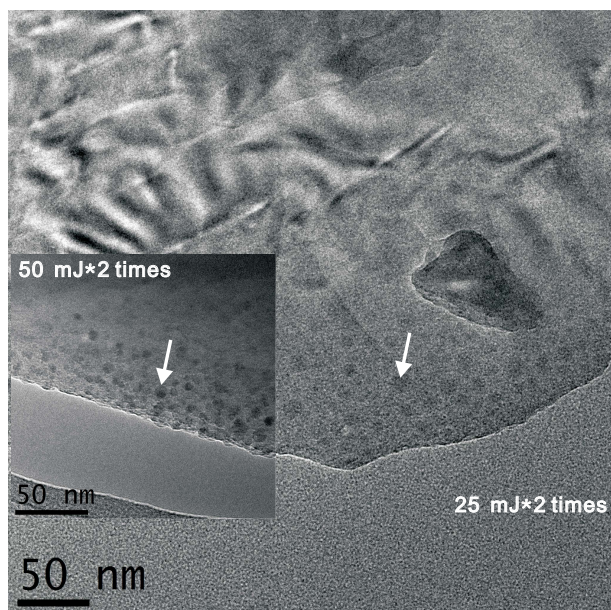


Fig. 14. TEM images of the olivine grains irradiated at 25 mJ for 2 times and at 50 mJ for 2 times (inset). The dark spots indicated by the white arrows are identified as iron particles. It is evident from this comparison that the npFe^0 particles produced at different energy levels in this work have similar size distributions (<30 nm).

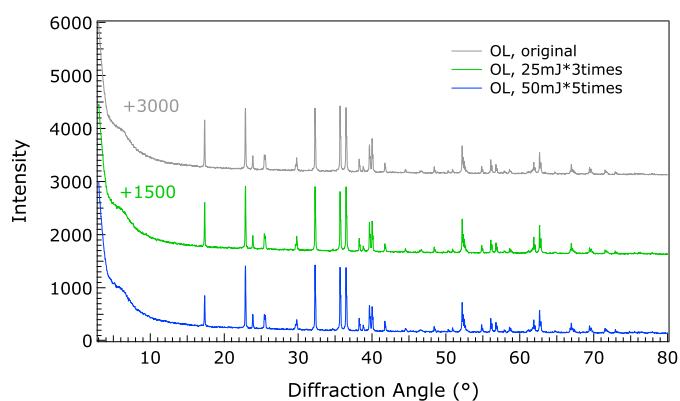


Fig. 15. XRD spectra of three typical olivine samples: the original olivine, olivine irradiated under 25 mJ/pulse for 3 times and olivine irradiated under 50 mJ/pulse for 5 times, respectively. The first two spectra are offset by an amount indicated by the numbers in graph for clarity.

amorphous layers are identified on the surfaces of irradiated olivine particles from TEM images, the XRD spectra did not show any detectable crystal structural changes.

Raman spectra. Figure 16 shows the typical Raman spectra measured under an excitation power of 9 mW. We have found that at this power the spectra have enough signal-to-noise ratios while no heating damage was incurred during measurements. The overall spectra are shown in Fig. 16a and the enlarged weaker bands are displayed in Fig. 16b with the intensities shifted upwards for clarity. Obviously, vibrational Raman modes have survived even in the most heavily irradiated samples and thus agree with the MIR and XRD results. More discussions on Raman features are presented in Sect. 4.3.

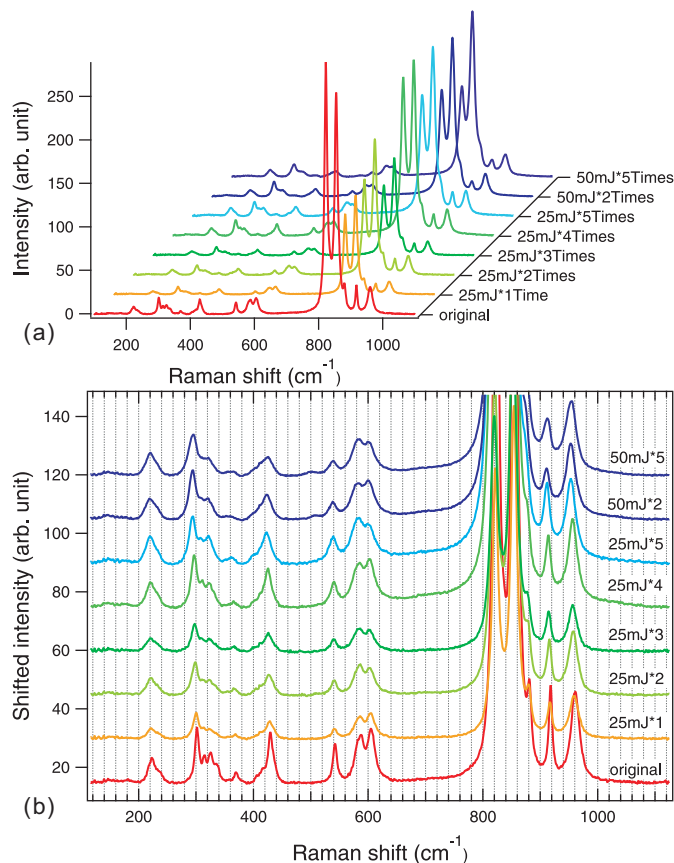


Fig. 16. Raman spectra of the original and the irradiated olivine samples. **a)** Waterfall plot of the sample spectra bands; **b)** the weaker bands that are shifted upwards for clarity.

3.2. Results of model predictions

The effects of npFe^0 on reflectance spectra. Since the irradiation-produced npFe^0 grains may either form a layer coating the particles or exist as scatters inside, their effects on optical properties need to be considered individually. For the first case, Fig. 17 shows model reflectance predictions of olivine covered by an npFe^0 coating with thickness varied from 0 to 1000 nm. The content of npFe^0 within the coating was set to a very high value of 1 vol. %. Both the Hapke model (Fig. 17a) and the DISORT (Fig. 17b) predictions show that the existence of npFe^0 result in an overall reduced reflectance, subdued absorption features, and a reddened VNIR spectra consistent with the previous pulsed laser irradiation experiments (e.g., Yamada et al. 1999; Sasaki et al. 2003). However, the MIR spectra remain essentially unchanged even when the npFe^0 coating thickness reaches 1000 nm. For the second case, Fig. 18 shows the modeled reflectance of npFe^0 uniformly distributed inside olivine grains (inset of Fig. 18a). As shown by both the Hapke model and the DISORT predictions, an amount of 0.01 vol.% npFe^0 is sufficient to cause appreciable feature changes in the VNIR spectra, while the MIR bands almost remain unchanged even when the npFe^0 contents reaches an unrealistically high level of 1 vol. % (Morris 1980).

The effects of amorphous layer. We next consider the effects of an amorphous layer coating the olivine particles by fixing the diameter of an olivine core of $30 \mu\text{m}$ and varying the coating thickness from 0 nm to 1000 nm. In addition to layer thickness

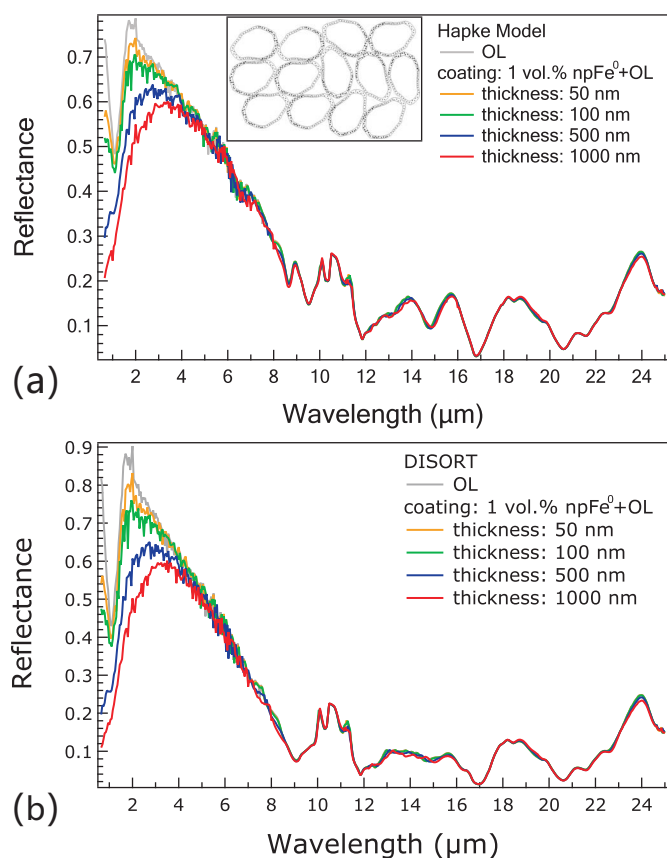


Fig. 17. Modeled reflectance of olivines with various thicknesses of npFe^0 coatings. **a)** Results of the Hapke Model; **b)** results of the DISORT. The inset in **a)** is a schematic showing the npFe^0 distribution patterns used in modelings. The content of npFe^0 in the coatings was set to be 1 vol. %.

effects, we also looked at the effects of four different compositions of the glassy coatings (see Sect. 2.2).

Figure 19 shows the reflectance predictions of olivine coated by Glass 1 (Fo_{95}). The modeled results indicate that the MIR spectra may be affected by glassy coating. The vibrational bands are weakened as the coating thickness increases, which is consistent with the MIR measurements on laser irradiated olivine particles. Although differences of CF positions exist between the two model predictions (Hapke model: $8.65 \mu\text{m}$; DISORT: $9.05 \mu\text{m}$), both models predict that the CF position slightly shifted ($0.05 \mu\text{m}$) to shorter wavelength when the coating is thick enough ($>500 \text{ nm}$). However, the shift is negligible when the layer thickness is smaller than 200 nm which is larger than the upper limit of the layers among the particle samples returned from Itokawa (Noguchi et al. 2011). Figure 20 shows the modeled spectra of olivine particles coated with Glass 2 which contains more Fe compared to Glass 1. Both models show that more Fe within the glassy coating darkens and reddens the VNIR spectra, similar to the effects produced by the npFe^0 . However, the MIR spectral feature changes incurred from a different Fe content (Glass 2 vs. Glass 1) are negligible as compared with the NIR feature changes. Figures 21 and 22 show the predicted spectra of olivine particles coated with Glass 3 and Glass 4, respectively. Compared with pyroxene-type glassy coatings (Glass 1 and Glass 2), olivine-type glass coatings (Glass 3 and Glass 4) make the CF position of olivine shift towards longer wavelength which is more consistent with our measurements. This may indicate that the glassy coating produced in our simulations are

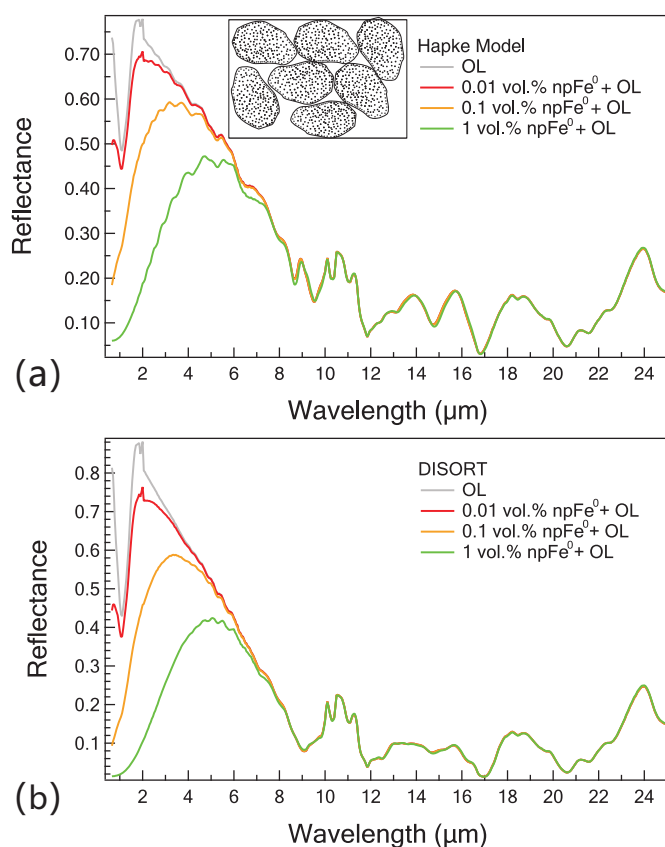


Fig. 18. Modeled reflectance of olivines with various contents of npFe^0 . **a)** Results of the Hapke Model; **b)** results of the DISORT. The npFe^0 is assumed to be evenly distributed in the grains as indicated by the inset in **a)**.

compositionally similar to olivine-type glass. Except for this difference, all four different glassy coatings caused similar darkening effects on the MIR spectra of olivine grains.

The broad peaks appearing between 2 and $8 \mu\text{m}$ in model predictions can be grouped into two categories: those redshift (Figs. 17, 18, 20 and 22) and those remain unshifted (Figs. 19 and 21) as glassy coating thickness or iron content increases. Specifically, redshifts and no-shifts occur in iron-rich and iron-poor environments, respectively. Unfortunately, the measured spectra in this region (Fig. 9a) are contaminated by the strong absorption of the reference gold mirror near $3 \mu\text{m}$ which prevents a decisive model/measurement comparison. Future work on this broad NIR feature is expected.

4. Discussions

4.1. VNIR spectral features

Our pulsed laser irradiation experiments have successfully reproduced the optical effects of space weathering in the VNIR region which are consistent with previous simulation results (e.g., Yamada et al. 1999; Sasaki et al. 2003). By performing TEM and EDS analysis, we identified two types of npFe^0 , one contained in the melted spherical particles (Fig. 10a) and the other one distributed in the rim of some olivine particles. These morphologies are very similar to the npFe^0 distributions in the returned lunar and Itokawa samples (e.g., Keller & McKay 1997; Noguchi et al. 2011). Most of the npFe^0 particles produced in our experiments are smaller than 10 nm in diameter. Although some npFe^0 particles can reach 30 nm in diameter in

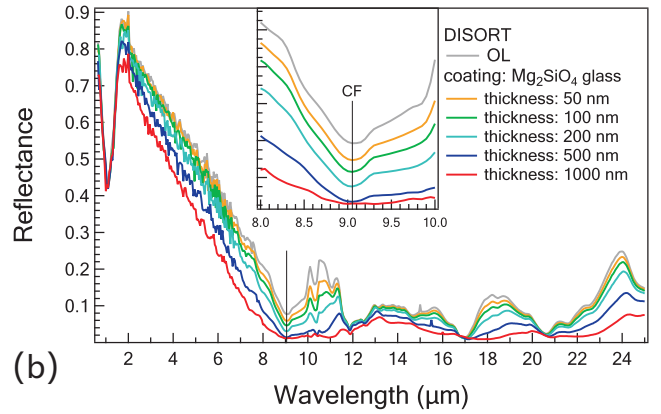
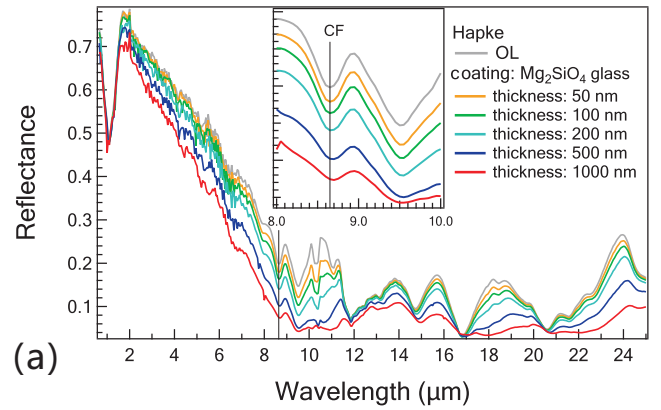
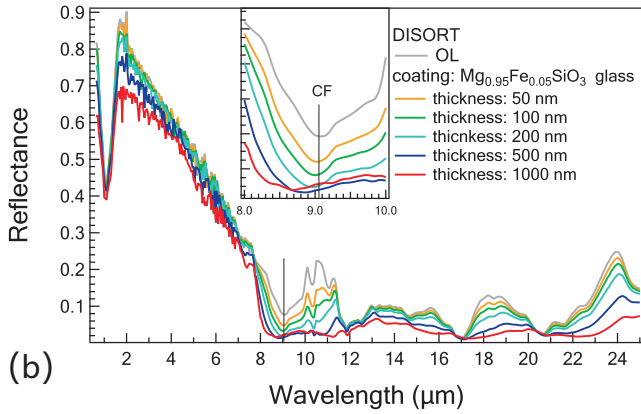
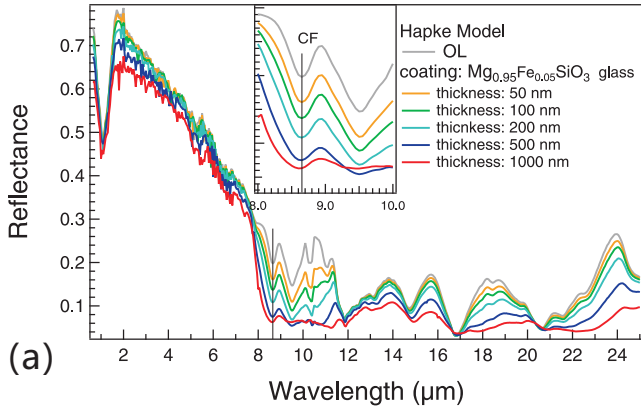


Fig. 19. Modeled reflectance of olivines coated by Glass 1. Predictions of the Hapke model **a)** and the DISORT **b)**. The insets are enlarged CF features and the vertical black lines indicate the CF positions of the uncoated olivine.

Fig. 21. Same as Fig. 19 but coated by Glass 3.

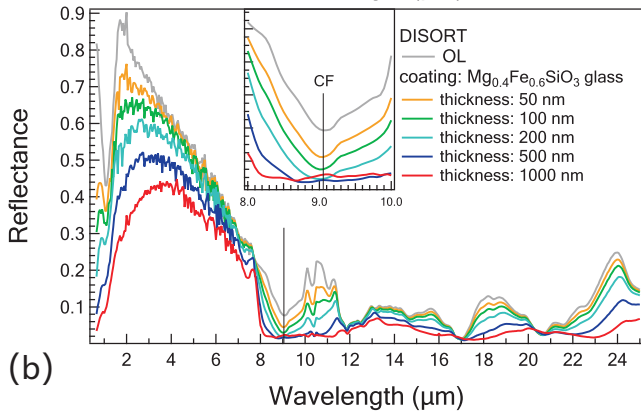
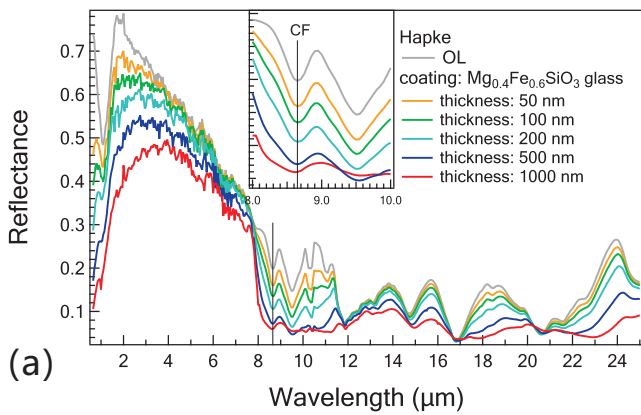


Fig. 20. Same as Fig. 19 but coated by Glass 2.

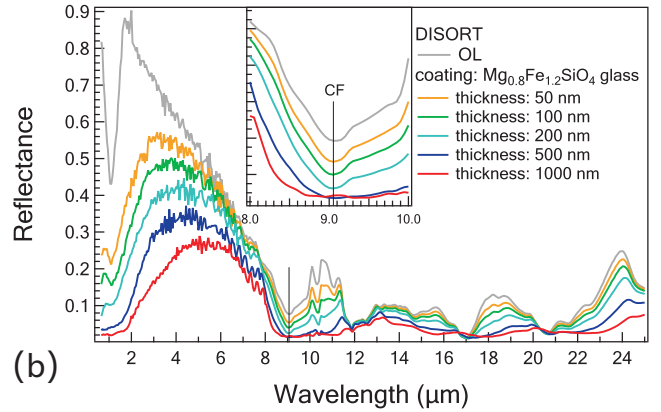
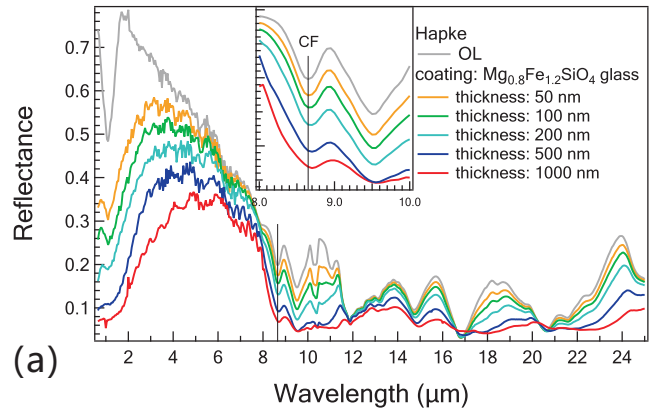


Fig. 22. Same as Fig. 19 but coated by Glass 4.

the aggregates after irradiation with 50 mJ/pulse for 5 times, they are still considerably smaller than the npFe⁰ found in returned lunar agglutinates (e.g., Pieters et al. 2000).

For the 25 mJ/pulse irradiation, our results indicate that the changes of the 1 μm band depth are proportional to number of irradiations, while Sasaki et al. (2003) shows that the spectral change could be saturated after being irradiated under 30 mJ/pulse for 5 times. Compared with Sasaki et al. (2003), we set a much slower scanning velocity (1 mm s⁻¹) compared to their 5 mm s⁻¹. As a result, the imparted energy of our one irradiation experiment in unit area is 750 mJ/mm² for 25 mJ/pulse which is much larger than their 240 mJ/mm² for 30 mJ/pulse. In terms of the total deposited energy, their five-time irradiation under 30 mJ/pulse is only equivalent to two-time irradiation under 25 mJ/pulse in our experiment. However, we did not find the similar saturation trend. Considering that the difference of the energy per pulse is small, the major difference between our results should be caused by the particle packing conditions, as Sasaki et al. (2003) irradiated packed grains in pellet form while we used loose powders. Thus it is likely that a compact surface would be more easily to be saturated in spectra changes. Therefore, the surface structure and laser scanning velocity must be carefully considered if we want to evaluate the real weathering duration through pulsed laser simulation experiments.

The above results imply that the weathering degree, as manifest by the darkening, reddening, and the subdued 1 μm absorption features, is not simply controlled by the total deposited energy, but also the single pulse energy. With increased number of irradiations, the spectral features tend to disappear (Fig. 5) and the overall spectrum approaches the continuum (Fig. 7a). However, when the sample irradiated with 25 mJ for 5 times (3750 mJ/mm² total deposited energy) is compared to that irradiated with 50 mJ for 2 times (3000 mJ/mm² total deposited energy), the latter one is found to have more significant darkening and more subdued spectral features but less reddening feature, though the latter one's total deposited energy is 750 mJ/mm² less. We have performed repeated experimentations to make sure the above variation trends can be reproduced reliably. This may indicate that spectral reddening is more susceptible to energy deposition rate (single pulse energy level) and could be explained by the argument that irradiations at higher energy deposition rate might produce larger npFe⁰ grains (>50 nm) that darken but not redden the spectra (Lucy & Riner 2011). However, the comparisons shown in Fig. 14 clearly demonstrate that the npFe⁰ grains produced at 50 mJ/pulse and 25 mJ/pulse in our simulations have commensurate size and are much smaller than 50 nm. Therefore, a more plausible explanation is that at higher energy deposition rate the weathered grains are coated by thicker glassy layers and thus any npFe⁰ induced reddening is greatly suppressed by darkening. Although we are unable to determine the actual layer thickness produced by 50 mJ/pulse irradiations, model predictions as shown in Fig. 22 clearly show that an iron-rich olivine-type glassy coating can significantly darken the VNIR spectra.

In the current study we ignored any possible npFe⁰ grain size effects on reflectance and this is a major shortcoming especially for VNIR model predictions. Although a modeling approach proposed by Lucy & Riner (2011) has accounted for the npFe⁰ particle size effect, it is only applicable to VNIR spectra as in this region the single scattering phase function can be approximated by a constant value. Moreover, Lucy & Riner (2011) found that the npFe⁰ grain size effects on modeling results are only significant at short wavelengths. As we have pointed out, we concentrate our model/measurement comparisons on MIR regions

where the radiation wavelength is much larger than the grain size of the npFe⁰ particles produced in our simulations (<30 nm), and thus ignoring the npFe⁰ size should not incur serious errors. The npFe⁰ grain size effects on VNIR spectra merit further investigations with controlled production of npFe⁰ with various size distributions.

4.2. MIR reflectance features

Group theoretical analysis yields totally 35 infrared-active vibrational modes for olivine crystal as 13B_{1u}+9B_{2u}+13B_{3u} (e.g., Paques-Ledent & Tarte 1973; Hofmeister 1987). Although mode assignment can be made by performing polarized reflectance measurements on aligned single crystals, it would be very difficult to identify the mode symmetry for each band in randomly orientated small grains as the B_{1u}, B_{2u} and B_{3u} modes appear in overlapping spectral regions and have similar spectral shapes (Hofmeister 1987). As a result, usually a band number instead of a specific irreducible representation is assigned to each distinct reflectance peak appearing in the MIR region of powdered samples. Comparisons of our measurement on unirradiated olivine sample with previous measurements (as summarized in Table 3 in Hamilton 2010) and lattice dynamics computations (Noel et al. 2006) give the following identifications (in cm⁻¹): 1070 (band 1), 988 (band 2), 964 (band 2a), 947 (band 3), 876 (band 3a), 853 (band 4, s), 777 (TF), 640 (band 5), 584 (band 5a), 557–546 (band 5s), 528 (band 6), 503 (band 7), 471 (band 8), 442 (band 8a, s), 417 (band 9) (s as shoulder). Table 3 summarizes the identifications in both wavenumbers and microns. Among these peaks, bands 1 to 4 and bands 5 to 8a belong to the stretching and bending of the SiO₄ group, respectively (Noel et al. 2006). Band 9 either belongs to relative motions between Fe and SiO₄ or SiO₄ bending (Noel et al. 2006). Nearly all bands have survived the heaviest irradiations (50 mJ/pulse for 5 times), as can be seen in Fig. 9. As Sect. 3.1 shows, the MIR reflectance spectral features of olivine are quite immune to the productions of npFe⁰. In the irradiated olivine particles, we have confirmed the existence of the npFe⁰ and the VNIR reflectance spectra of these olivine samples changed a lot. However, nearly all major MIR vibrational features are retained even after the heaviest irradiation process under 50 mJ/pulse for 5 times which may be “over-irradiated” as compared with real space weathering processes on asteroids (e.g., Clark et al. 2002; Chapman 2004).

The reflectance modeling results show that the MIR spectra of olivine are not susceptible to npFe⁰, even when the npFe⁰ content reaches an unrealistic high level of 1 vol. % (Morris 1980). In contrast, amorphous coatings darken and weaken the vibrational bands more efficiently, as revealed by both the TEM/MIR measurements and the Hapke and the DISORT model predictions. Moreover, an olivine-type glassy coating (Mg_xFe_{2-x}SiO₄) may shift the CF position of olivine towards longer wavelength when the coating is thick enough. However, as long as the glassy coating thickness is less than 200 nm, which is much larger than the upper value of returned asteroid samples, the CF position and other MIR features are very well retained. It is also found that the effects of irradiations with 25 mJ/pulse on the MIR spectra are rather limited. This may occur because low energy deposition rate did not produce thick enough coatings.

Recently Lucy et al. (2016) found the Christiansen Feature of more space-weathered lunar surface shifts to longer wavelength as compared to less weathered area based on Diviner observations over the Moon, though the magnitude of the shift is only a few percent of one micron. Although our reflectance

Table 3. MIR Band positions of olivines before and after irradiations in wavenumbers (upper) and microns (lower).

OL*	CF	Band 1	Band 2	Band 2a	Band 3	Band 3a	Band 4	TF	Band 5	Band 5a	Band 5s	Band 6	Band 7	Band 8	Band 8a, s	Band 9
0	1115	1070	988	964	947	876	853	777	640	584	557–546	528	503	471	442	417
1	1117	1070	988	964	947	878	853	775	640	584	557–546	528	503	471	442	417
2	1113	1070	989	964	947	878	853	777	638	586	557–546	527	503	469	442	415
3	1113	1070	989	964	947	876	851	775	644	584	557–546	528	501	471	442	415
4	1113	1070	989	964	947	878	853	775	640	586	557–546	528	501	467	442	419
5	1113	1070	989	964	945	880	853	775	638	586	557–546	527	501	473	442	415
6	1115	1069	989	964	947	878	853	777	640	590	557–546	527	503	469	442	419
7	1109	1065	989	964	945	880	853	785	635	590	557–546	523	501	469	442	413

OL*	CF	Band 1	Band 2	Band 2a	Band 3	Band 3a	Band 4	TF	Band 5	Band 5a	Band 5s	Band 6	Band 7	Band 8	Band 8a, s	Band 9
0	8.97	9.34	10.13	10.37	10.56	11.42	11.73	12.87	15.62	17.11	17.94	18.92	19.87	21.25	22.542	24.00
1	8.95	9.34	10.13	10.37	10.56	11.40	11.73	12.90	15.62	17.11	17.94	18.92	19.87	21.25	22.542	24.00
2	8.99	9.34	10.11	10.37	10.56	11.40	11.73	12.87	15.66	17.06	17.94	18.99	19.87	21.34	22.542	24.12
3	8.99	9.34	10.11	10.37	10.56	11.42	11.76	12.90	15.52	17.11	17.94	18.92	19.94	21.25	22.542	24.12
4	8.99	9.34	10.11	10.37	10.56	11.40	11.73	12.90	15.62	17.06	17.94	18.92	19.94	21.42	22.542	23.89
5	8.99	9.34	10.11	10.37	10.58	11.37	11.73	12.90	15.66	17.06	17.94	18.99	19.94	21.16	22.542	24.12
6	8.97	9.36	10.11	10.37	10.56	11.40	11.73	12.87	15.62	16.94	17.94	18.99	19.87	21.34	22.542	23.89
7	9.02	9.39	10.11	10.37	10.58	11.37	11.73	12.74	15.76	16.94	17.94	19.13	19.94	21.34	22.542	24.23

Notes. (*) The numbers indicate the olivines with different irradiation degrees: 0 (unirradiated); 1 (25 mJ/pulse \times 1 time); 2 (25 mJ/pulse \times 2 times); 3 (25 mJ/pulse \times 3 times); 4 (25 mJ/pulse \times 4 times); 5 (25 mJ/pulse \times 5 times); 6 (50 mJ/pulse \times 2 times); 7 (50 mJ/pulse \times 5 times)

Table 4. Raman mode assignments of the olivine samples based on Kolesov & Geiger (2004).

OL*	Ag	B3g	B2g	Ag	Ag	Ag	B1g+B2g+B3g	Ag	B1g+B2g	B3g?	Ag	Ag	B1g+B3g	Ag	Ag
0	961	918	881	855	823	605	588	542	430	369	336(s)	326	315	301	223
1	958	917	879	854	822	605	586	541	429	368	–	323	314	300	222
2	958	916	878	853	821	602	587	541	426	365	–	323	314	298	222
3	957	914	~877(s)**	852	820	603	586	541	426	366	–	322	~311	298	220
4	956	914	~875(s)	852	819	602	585	541	426	365	–	323	311	297	220
5	953	912	~872(s)	851	817	599	584	539	423	361	–	322	308	295	220
6	953	911	~874(s)	851	817	600	584	538	423	359	–	321	~308	294	219
7	955	912	~874(s)	851	819	599	585	539	426	365	–	321	–	296	221

Notes. (*) The sample numbers are the same as those used in Table 3; (**): s: shoulder.

measurements were carried out in ambient environment, the band positions summarized in Table 3 suggest that the CF positions of the heavily irradiated samples indeed have shifted to longer wavelengths, from 8.97 μm for unirradiated sample to 9.02 μm for 50 mJ/pulse 5 times (the 4 cm^{-1} spectral resolution in the MIR region used in our measurements translates to 0.04 μm in wavelength scale). For bands other than the CF and the TF, many bands exhibit a redshift of several wavenumbers upon irradiations. This is consistent with the Raman results shown in 4.3 and should be caused by the tensile strain induced mode softening (Cerqueira et al. 1972) due to the presence of lattice defects upon irradiations.

4.3. Raman spectral features

As summarized in Table 4, out of the total 36 vibrational Raman modes for olivine crystal, $11A_g+7B_{1g}+11B_{2g}+7B_{3g}$, 14 peaks have been identified by comparing with previous powdered sample measurements (Kolesov & Geiger 2004). Laser irradiations caused two major spectral feature changes. First, the full width at half maximum (FWHM) of all Raman peaks increased upon irradiations (Fig. 16b). Second, upon irradiations all Raman modes experienced downshifts or mode softening

by 4–6 cm^{-1} (Table 4). These two features are strong indications of the presence of lattice defects after irradiations. The increase of the FWHM should be caused by the presence of glassy (amorphous) materials produced during the irradiation. The mode softening may be caused by coatings of crystalline olivine grains composed of nanophase irons and glassy materials, as tensile strains caused by lattice defects are known to downshift the Raman peaks (Cerqueira et al. 1972). However, the crystalline Raman features are very well preserved even under the most intense irradiations. This is quite consistent with the MIR and XRD features and thus we conclude that the crystal lattice survived the strong irradiations.

5. Conclusions

By performing pulsed laser irradiations on olivine grains with various energy levels and time durations, we have successfully reproduced the typical space weathering-induced reddening and darkening effects in the VNIR reflectance spectra. Based on the TEM analysis, we have identified the production of npFe^0 , and the iron grains are much smaller than 30 nm.

When using pulsed laser irradiation to simulate the micrometeorite impacts, the energy level should be carefully considered. Two different energy levels, 25 mJ and 50 mJ, have resulted in

two different variation trends of the VNIR spectral features as the number of irradiations increases. Irradiations at 25 mJ for 1 to 5 times have produced progressively overall shallower 1 μm band depth, lower albedo, and redder spectral slope. Irradiations at 50 mJ levels, however, produced pronounced darkening but less reddening. Since the TEM images show that irradiations at both levels have produced iron grains with similar size distributions (<30 nm), the difference must have been caused by thicker iron-bearing glassy layers produced at higher energy levels. Although the npFe^0 abundances produced by 50 mJ levels are higher than that produced by 25 mJ levels, the reddening effects caused by npFe^0 must have been suppressed by thicker amorphous layers which have profound darkening effects on reflectance.

In contrast to the visible and near-infrared spectra, MIR spectral features are much more immune to the intense irradiations. Although the Christiansen Feature and many reflectance bands show a redshift of up to 6 cm^{-1} under the most intense irradiations, the overall spectral features can survive the strongest irradiations which may be much more intense than the realistic micrometeorite bombardment levels on asteroid surface (e.g., Clark et al. 2002; Markley & Kletetschka 2016). The much lower MIR reflectance of samples irradiated at 50 mJ as compared with that irradiated at 25 mJ is again attributed to the thicker amorphous layers produced at higher energy irradiations.

Reflectance modeling results indicate that the MIR features are not susceptible to the productions of the npFe^0 and as long as the glassy coating thickness is less than 200 nm the CF position and other spectral features can be retained. The fact that the olivine crystal structure can survive heavy irradiations is supported by XRD and Raman scattering measurements. No detectable crystal structural changes were found in the XRD spectra of heavily irradiated samples. Although Raman peaks of the heavily irradiated samples show broadening and redshifts compared with the original sample, indicating the productions of glassy materials, lattice defects, and tensile stress, all vibrational modes can be clearly recognized.

As pyroxene is known to be more resistant to space weathering modifications (Yamada et al. 1999), the current results show that MIR spectral features may be very useful in remotely identifying the surface mineralogical compositions of airless bodies undergoing strong space weathering modifications.

Acknowledgements. We thank Sho Sasaki for helpful suggestions in the pulsed laser simulation system setup and Weidong Jin for programming the translation stage. Constructive reviews by Tomáš Kohout improved the quality of the manuscript. This work was supported by the National Natural Science Foundation of China (U1631124, 11573058, 11327303) and by the Fundamental Research Funds for the Central Universities, China University of Geosciences (Wuhan).

References

- Beichman, C., Bryden, G., Gautier, T., et al. 2005, *ApJ*, **626**, 1061
- Berger, E. L., & Keller, L. P. 2015, in *LPSC*, 46th Lunar and Planetary Science Conference, 2351
- Bohren, C. F., & Huffman, D. R. 2008, in *Absorption and scattering of light by small particles* (John Wiley & Sons)
- Britt, D., Kohout, T., Schelling, P., & Consolmagno, G. J. 2014, in *AAS/DPS Meeting*, 46
- Brucato, J., Strazzulla, G., Baratta, G., & Colangeli, L. 2004, *A&A*, **413**, 395
- Brunetto, R., Romano, F., Blanco, A., et al. 2006, *Icarus*, **180**, 546
- Burns, R. G. 1993, *Mineralogical applications of crystal field theory* (Cambridge University Press)
- Cerdeira, F., Buchenauer, C., Pollak, F. H., & Cardona, M. 1972, *Phys. Rev. B*, **5**, 580
- Chapman, C. R. 1996, *Meteorit. Planet. Sci.*, **31**, 699
- Chapman, C. R. 2004, *Annu. Rev. Earth Planet. Sci.*, **32**, 539
- Clark, R. N., & Roush, T. L. 1984, *J. Geophys. Res.: Solid Earth*, **89**, 6329
- Clark, B. E., Hapke, B., Pieters, C., & Britt, D. 2002, *Asteroids III*, eds. W. F. Bottke Jr., A. Cellino, P. Paolisci, & R. P. Binzel (Tucson: University of Arizona Press), 585
- Denevi, B., Lucey, P., & Sherman, S. 2008, *J. Geophys. Res.: Planets*, **113**, E02003
- Dorschner, J., Begemann, B., Henning, T., Jaeger, C., & Mutschke, H. 1995, *A&A*, **300**, 503
- Fabian, D., Jäger, C., Henning, T., Dorschner, J., & Mutschke, H. 2000, *A&A*, **364**, 282
- Fabian, D., Henning, T., Jäger, C., et al. 2001, *A&A*, **378**, 228
- Fulvio, D., Brunetto, R., Vernazza, P., & Strazzulla, G. 2012, *A&A*, **537**, L11
- Gaffey, M. J. 2010, *Icarus*, **209**, 564
- Hamilton, V. E. 2010, *Chem. Erde-Geochem.*, **70**, 7
- Hapke, B. 1973, *The Moon*, **7**, 342
- Hapke, B. 1981, *J. Geophys. Res.: Solid Earth*, **86**, 3039
- Hapke, B. 2001, *J. Geophys. Res.: Planets*, **106**, 10039
- Hapke, B. 2012, *Theory of reflectance and emittance spectroscopy* (Cambridge University Press)
- Hapke, B. 2013, *J. Quant. Spectr. Rad. Transf.*, **116**, 184
- Hapke, B., Cassidy, W., & Wells, E. 1975, *The Moon*, **13**, 339
- Hofmeister, A. M. 1987, *Phys. Chem. Miner.*, **14**, 499
- Jäger, C., Mutschke, H., Begemann, B., Dorschner, J., & Henning, T. 1994, *A&A*, **292**, 641
- Keller, L. P., & McKay, D. S. 1993, *Science*, **261**, 1305
- Keller, L. P., & McKay, D. S. 1997, *Geochim. Cosmochim. Acta*, **61**, 2331
- Kohout, T., Čuda, J., Filip, J., et al. 2014, *Icarus*, **237**, 75
- Kolesov, B., & Geiger, C. 2004, *Phys. Chem. Miner.*, **31**, 142
- Kuhlman, K. R., Sridharan, K., & Kvit, A. 2015, *Planet. Space Sci.*, **115**, 110
- Lawrence, S. J., & Lucey, P. G. 2007, *J. Geophys. Res.: Planets*, **112**, E07005
- Loeffler, M., Baragiola, R., & Murayama, M. 2008, *Icarus*, **196**, 285
- Lucey, P. G., & Riner, M. A. 2011, *Icarus*, **212**, 451
- Lucey, P. G., Greenhagen, B. T., Song, E., et al. 2016, *Icarus*, **283**, 343
- Marchi, S., Brunetto, R., Magrin, S., Lazzarin, M., & Gandolfi, D. 2005, *A&A*, **443**, 769
- Markley, M., & Kletetschka, G. 2016, *Icarus*, **268**, 204
- Miller, K. A., De Ruelle, N., Harlow, G., Domingue, D. L., & Savin, D. W. 2014, in *AAS Meet.*, 224
- Mishchenko, M. I., Dlugach, J. M., Yanovitsku, E. G., & Zakharova, N. T. 1999, *Morris*, R. 1980, in *LPSC*, **11**, 1697
- Mustard, J. F., & Hays, J. E. 1997, *Icarus*, **125**, 145
- Nesvorný, D., Jedicke, R., Whiteley, R. J., & Ivezić, Ž. 2005, *Icarus*, **173**, 132
- Noel, Y., Catti, M., D'Arco, P., & Dovesi, R. 2006, *Phys. Chem. Miner.*, **33**, 383
- Noguchi, T., Nakamura, T., Kimura, M., et al. 2011, *Science*, **333**, 1121
- Ordal, M. A., Bell, R. J., Alexander, R. W., Newquist, L. A., & Querry, M. R. 1988, *Appl. Opt.*, **27**, 1203
- Paques-Ledent, M. T., & Tarte, P. 1973, *Spectrochim. Acta A*, **29**, 1007
- Pieters, C. M. 1998, *Int. Geol. Rev.*, **40**, 981
- Pieters, C. M. 2002, in *LPI Mars Spectral Workshop II, 33rd Annual Lunar and Planetary Science Conf.*, March 11–15, Houston, Texas, 177
- Pieters, C. M., Taylor, L. A., Noble, S. K., et al. 2000, *Meteorit. Planet. Sci.*, **35**, 1101
- Poulet, H., & Mathieu, J. P. 1976, *Vibration spectra and symmetry of crystals* (Gordon & Breach Science Pub.)
- Quirantes, A., & Bernard, S. 2004, *J. Quant. Spectr. Rad. Transf.*, **89**, 311
- Salisbury, J. W., Basu, A., & Fischer, E. M. 1997, *Icarus*, **130**, 125
- Sasaki, S., Nakamura, K., Hamabe, Y., Kurahashi, E., & Hiroi, T. 2001, *Nature*, **410**, 555
- Sasaki, S., Hiroi, T., Nakamura, K., et al. 2002, *Adv. Space Res.*, **29**, 783
- Sasaki, S., Kurahashi, E., Yamanaka, C., & Nakamura, K. 2003, *Adv. Space Res.*, **31**, 2537
- Shkuratov, Y., Kaydash, V., Korokhin, V., et al. 2012, *J. Quant. Spectr. Rad. Transf.*, **113**, 2431
- Stammes, K., Tsay, S.-C., Wiscombe, W., & Laszlo, I. 2000, *DISORT*, Goddard Space flight center, NASA
- Tang, H., Wang, S., & Li, X. 2012, *Planet. Space Sci.*, **60**, 322
- Taylor, L. A., Pieters, C. M., Keller, L. P., Morris, R. V., & McKay, D. S. 2001, *J. Geophys. Res.: Planets*, **106**, 27985
- Vernazza, P., Carry, B., Emery, J., et al. 2010, *Icarus*, **207**, 800
- Yamada, M., Sasaki, S., Nagahara, H., et al. 1999, *Earth Planets Space*, **51**, 1255
- Zhang, H., & Voss, K. J. 2011, *Icarus*, **215**, 27
- Zhang, H., Yang, Y., Jin, W., Liu, C., & Hsu, W. 2014, *Opt. Express*, **22**, 21280